INORGANIC CHEMISTRY FRONTIERS

RESEARCH ARTICLE

View Article Online
View Journal | View Issue

Cite this: *Inorg. Chem. Front.*, 2022, **9**, 6237

Plasma-assisted rhodium incorporation in nickel–iron sulfide nanosheets: enhanced catalytic activity and the Janus mechanism for overall water splitting†

Junying Li,[a] Xiaodeng Wang,*[b] Lingya Yi,[a] Changxiang Fang,[a] Tianhao Li,[a] Wei Sun*[c] and Weihua Hu*[a]

NiFe catalysts show compelling oxygen evolution reaction (OER) activity in alkaline solution but their hydrogen evolution reaction (HER) activity is limited. In this work Rh was incorporated in Fe-doped Ni_3S_2 nanosheets with the assistance of hydrogen plasma to significantly enhance the HER/OER catalytic activity. The resultant catalyst, *p*-Rh/Fe-Ni_3S_2/NF, was composed of Rh/Rh_2S_3 heterostructured clusters embedded in Fe-Ni_3S_2 nanosheets; it needs overpotentials of only 108 and 237 mV to achieve HER and OER currents of 100 mA cm^{-2}, respectively, and drives overall water splitting at 1.79 V with a current of 100 mA cm^{-2} as a bifunctional catalyst. Post-characterization and density functional theory (DFT) calculation reveal its *operando* evolution behavior and a unique Janus catalytic mechanism for the HER and OER. For the HER, a Rh/Rh_2S_3 heterointerface with strong H_2O adsorption energy and optimal H adsorption energy is the active site; in the OER, it experiences surface transformation under *operando* conditions; an *in situ* formed Rh/Fe-doped NiOOH layer with strengthened binding of *O facilitates the rate determining step of *O formation to accelerate the OER process. Hydrogen plasma treatment not only helps partially reduce Rh to form HER-active Rh/Rh_2S_3 heterostructures but also induces rich defects/vacancies to facilitate surface reconstruction/phase transformation to form an active co-doped NiOOH phase under OER conditions. This work may shed light on the promotive role of noble metals on NiFe-based catalysts for water splitting.

Received 30th July 2022,
Accepted 5th October 2022

DOI: 10.1039/d2qi01655a

rsc.li/frontiers-inorganic

1. Introduction

Electricity-driven water splitting to hydrogen fuel is one of the promising techniques for sustainable grid-scale energy storage.[1] For high energy efficient water splitting, it is an urgent task to explore active electrocatalysts with low content/free of precious metals for its two sluggish half-reactions, namely hydrogen evolution reaction (HER) and oxygen evolution reaction (OER).[2,3] Ni/Fe based materials have been the focus of intensive research for years due to their excellent OER activity in alkaline solution.[4,5] Most of these catalysts experience *operando* surface reconstruction and the *in situ* formed Fe-doped nickel oxyhydroxide (NiOOH) phase is the real active phase.[6,7] The Fe atoms in these catalysts, either added on purpose or incidentally as contaminants, are found to be critical for the overall OER activity while the NiOOH provides a suitable matrix for dynamic balance.[8,9] Despite their excellent OER activity, Ni/Fe catalysts possess low HER activity as a consequence of weak hydrogen adsorption.[10] To enhance their HER activity for possible Janus/bifunctional electrocatalysis in water electrolysis, bimetal phosphides and sulfides were synthesized but their HER catalytic performance is far from satisfactory.[11,12]

In recent years a new strategy has been emerging by introducing Pt-group metals in the form of single-atom dopants, clusters or nanoparticles into NiFe catalysts to further boost their OER while significantly improving their HER performance.[10,13,14] For the OER, precious metal species in the high valence state were stabilized by the NiFe matrix to accelerate the O–O bond formation; the adsorption energy of multiple

[a]*Key Laboratory of Luminescent and Real-Time Analytical Chemistry (Southwest University), Ministry of Education, School of Materials and Energy, Southwest University, Chongqing 400715, China. E-mail: whhu@swu.edu.cn*
[b]*Chongqing Engineering Research Center of New Energy Storage Devices and Applications, Chongqing University of Arts and Sciences, Chongqing, 402160, China. E-mail: wangxd@cqwu.edu.cn*
[c]*Key Laboratory of Laser Technology and Optoelectronic Functional Materials of Hainan Province, Key Laboratory of Functional Materials and Photoelectrochemistry of Haikou, College of Chemistry and Chemical Engineering, Hainan Normal University, Haikou 571158, China. E-mail: sunwei@hainnu.edu.cn*

†Electronic supplementary information (ESI) available: DFT calculation details, SEM images, SAED, XPS, CV, LSV, TEM images, XRD patterns, and faradaic efficiency. See DOI: https://doi.org/10.1039/d2qi01655a

oxygen-containing intermediates was also optimized.[15,16] For the HER, the appropriate hydrogen adsorption energy of Pt-group metal enables fast hydrogen evolution while the NiFe matrix as a co-catalyst enables fast water dissociation in alkaline solution.[10,17,18] Although the detailed mechanism remains controversial, these encouraging works point to an intriguing direction for the rational design of bifunctional catalysts for water splitting.

Heazlewoodite (Ni_3S_2) is a naturally occurring mineral and inspires considerable research interest for water splitting due to its intrinsically high conductivity and rich yet well-controllable nanostructures.[19,20] Its OER and HER performance were manipulated and explored *via e.g.*, engineering of high-index facets, incorporation of other metallic sulfide/oxide nanoparticles, *etc*.[19,21,22] However, their electrocatalytic performance needs improvement for practical applications.

In this work, a highly active bifunctional catalyst was reported for alkaline water electrolysis by incorporating Rh in Ni_3S_2 nanosheets on Ni foam with the assistance of hydrogen plasma. As-synthesized catalyst (denoted as *p*-Rh/Fe-Ni_3S_2/NF) shows outstanding OER and HER activity; it reaches an OER/HER current density of 100 mA cm^{-2} at overpotentials of 237 mV and 108 mV, respectively. Its OER/HER activities do not fade significantly after more than 50 h of operation at a high current of 100 mA cm^{-2}, showing excellent durability. Detailed post-catalysis characterization and density functional theory (DFT) calculation reveal its unique Janus catalytic mechanism behind the Rh-enhanced OER and HER activity.

2. Experimental

2.1 Synthesis of *p*-Rh/Fe-Ni_3S_2/NF and other catalysts

A piece of Ni foam (NF, 3 cm × 4 cm × 1.5 mm) was washed with deionized (DI) water, acetone, and 1 M of HCl for 30 min in sequence. It was then immersed in a mixed solution containing 20 mL of DMF, 8 mL of anhydrous ethanol, thioacetamide (TAA, 100 mg), $Ni(NO_3)_2{\cdot}6H_2O$ (0.768 mmol), and $FeCl_3$ (0.192 mmol) and transferred into a Teflon-lined stainless-steel autoclave. The autoclave was heated to 150 °C for 6 h in an electric oven. The NF was washed with DI water and dried at 60 °C to obtain Fe-Ni_3S_2/NF.

As-synthesized Fe-Ni_3S_2/NF was immersed in a solution containing 10 mL of DI water, 20 μL of ethylene glycol, and 200 μL of $RhCl_3{\cdot}xH_2O$ (25 mg mL^{-1}) in a centrifuge tube. The tube was sealed and gently shaken for 48 h at room temperature. After washing and drying at 60 °C in a vacuum, the Rh/Fe-Ni_3S_2/NF was prepared.

As-synthesized Rh/Fe-Ni_3S_2/NF was placed in the reaction chamber with a pure H_2 atmosphere under a pressure of 18 Pa. At a H_2 flow rate of 30 mL min^{-1}, the hydrogen plasma was activated with an RF power at 45 W for 20 min treatment to obtain *p*-Rh/Fe-Ni_3S_2/NF.

As-synthesized Rh/Fe-Ni_3S_2/NF was placed in a tube furnace with H_2/Ar (5 : 95) at 350 °C for 2 h for annealing. After cooling to room temperature, Rh/Fe-Ni_3S_2/NF-350 was prepared.

2.2 Preparation of RuO_2/NF and Pt/C/NF

RuO_2 (2 mg, 99.9 wt% from Alfa-Aesar) and Pt/C (2 mg, 20 wt% from Alfa-Aesar) were respectively suspended in a mixture of absolute ethanol (985 μL) and Nafion (15 μL) to form a homogeneous catalyst ink under ultrasonication. Then the ink was dispersed onto NF (1 cm × 1 cm) and dried at room temperature in a vacuum. The final RuO_2 and Pt loadings are ~2 mg cm^{-2} and 0.4 mg cm^{-2}, respectively.

2.3 Material characterization

The scanning electron microscopy (SEM) images of all samples were observed on a field emission SEM from JEOL (JSM-7800F). Transmission electron microscopy (TEM) observation was carried out on a JOEL TEM-2100 system after ultrasonically peeling off the materials from NF. The crystalline structures were probed by X-ray diffraction (XRD, Shimadzu XRD-7000 diffractometer with Cu Kα line). X-ray photoelectron spectroscopy (XPS) measurement was performed on an ESCALAB 250Xi system from Thermo Fisher. Inductively coupled plasma atomic emission spectrometry (ICP-AES) measurements were performed on a PerkinElmer Optima 8000. Raman spectra were acquired using a LabRAM HR Evolution confocal Raman microscope from Horiba Jobin Yvon with a 50× objective (LMPlanFL N 50×/0.50, Olympus). A laser of 532 nm with a power of 1 mW was used as the excitation light. Before measurements, the spectral shifts were calibrated using the 520.7 cm^{-1} peak of silicon. For electrochemical *in situ* Raman spectra, the catalyst was deposited on a graphitic rod as a working electrode. A graphitic rod counter electrode and a Hg/HgO reference electrode combined with a 760E potentiostat from CH Instruments, Shanghai, were employed for electrochemical measurements. Raman spectra were recorded from 300 to 1000 cm^{-1} at a resolution of 0.5 cm^{-1}.

2.4 Electrochemical measurements

All electrochemical experiments were tested using a 760E workstation (CH Instrument, USA) under a three-electrode setup. Freshly prepared 1.0 M KOH was used as the electrolyte solution. A graphite rod and a carefully calibrated Hg/HgO were used as the counter electrode and the reference electrode, respectively. All polarization curves were collected at a scan rate of 5 mV s^{-1} and presented after *iR* compensation unless otherwise specified. The electrochemical double-layer capacitance of a catalyst was estimated by the slope of a linear curve between non-faradaic capacitive current *vs.* scanning rate. The electrochemical surface area (ECSA) of a catalyst was calculated from the double-layer capacitance according to the equation, ECSA = C_{dl}/C_s, where C_s is the specific capacitance of a planar surface and is selected as 0.04 mF cm^{-2} in the present work.[23] Electrochemical impedance spectroscopy (EIS) measurements were carried out with an amplitude of 5 mV in the frequency range from 100 kHz to 0.01 Hz. Alkaline electrolyzer measurement was carried out in a standard two-electrode system without *iR* compensation.

2.5 DFT calculation

All DFT calculations were conducted using the Vienna *ab initio* simulation package (VASP). The generalized gradient approximation (GGA) functional of Perdew, Burke, and Ernzerhof (PBE) was employed for the electron exchange and correlation energy for structural relaxation.[24] The cut-off energy of plane-wave basis was set as 450 eV. The convergence criterion of total energy was converged to 1.0×10^{-4} eV per atom, and that of force on every atom was smaller than 0.02 eV $Å^{-1}$. A vacuum width of 15 Å along the *Z* axis was created to ensure negligible interaction.

3. Results and discussion

3.1. Characterization of *p*-Rh/Fe-Ni_3S_2/NF

As illustrated in Fig. 1a, *p*-Rh/Fe-Ni_3S_2/NF was synthesized *via* a three-step strategy. Fe-doped Ni_3S_2 nanosheets were first grown on NF (designated as Fe-Ni_3S_2/NF) *via* a hydrothermal reaction. After that, Rh atoms were impregnated on Fe-Ni_3S_2 nanosheets by immersing in $RhCl_3$ solution to obtain Rh/Fe-Ni_3S_2/NF. The driving force behind this incorporation is associated with the cation exchange and/or hetero-epitaxial growth of Rh_2S_3.[25] In the third step, Rh/Fe-Ni_3S_2/NF was processed in hydrogen plasma for 20 min to obtain *p*-Rh/Fe-Ni_3S_2/NF. The Rh loading is ~44 μg cm^{-2} on the resultant *p*-Rh/Fe-Ni_3S_2/NF catalyst as measured by ICP-AES.

Fe-Ni_3S_2/NF shows dense and uniform nanosheets vertically grown on the NF skeleton and these ultrathin nanosheets interconnect with each other to form a porous layer (see the SEM image on the left in Fig. 1a). After Rh^{3+} impregnation, these nanosheets retained their morphology in Rh/Fe-Ni_3S_2/NF (SEM image in the middle in Fig. 1a). After hydrogen plasma treatment, remarkably the space between the nanosheets becomes larger on resultant *p*-Rh/Fe-Ni_3S_2/NF (SEM image on the right in Fig. 1a); the lateral planes of nanosheets were destroyed, leaving behind the nanoframes with rough surfaces and increased thicknesses (see high-resolution SEM images in Fig. S1†). The morphological change is more obvious with prolonged treatment duration (Fig. S1†), suggesting the reconstruction of the nanosheets in hydrogen plasma due to the etching effect of highly corrosive H species produced *via* the ionization of H_2.[26,27] This unique reticular structure of *p*-Rh/Fe-Ni_3S_2/NF is beneficial for mass transport and offers a large specific surface area for expediting the electrochemical reactions.[28–30]

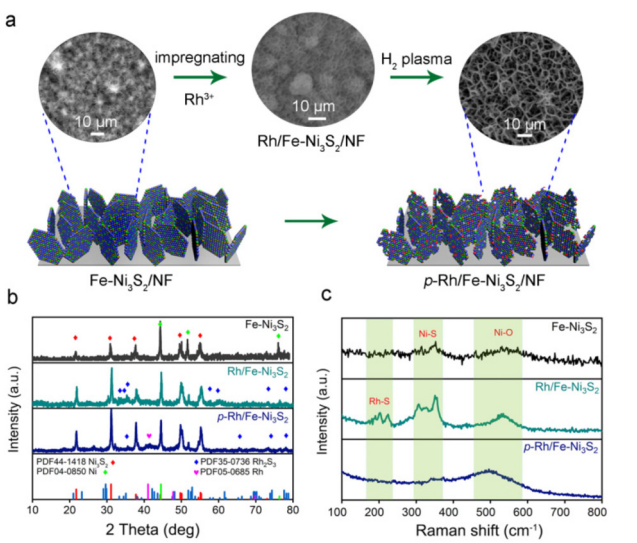

Fig. 1 (a) Schematic illustration of the three-step synthesis of *p*-Rh/Fe-Ni_3S_2/NF with SEM images of Fe-Ni_3S_2/NF (left), Rh/Fe-Ni_3S_2/NF (middle), and *p*-Rh/Fe-Ni_3S_2/NF (right); (b) XRD patterns and (c) Raman spectra of Fe-Ni_3S_2/NF, Rh/Fe-Ni_3S_2/NF, and *p*-Rh/Fe-Ni_3S_2/NF.

In the XRD pattern, all diffraction peaks of Fe-Ni_3S_2/NF nanosheets are well indexed to the rhombohedral phase Ni_3S_2 (PDF no. 44-1418) and metallic Ni (from NF substrate, PDF no. 04-0850, Fig. 1b). After incorporation of Rh, new diffraction peaks from the Rh_2S_3 phase (PDF no. 35-0736) appear besides those from Ni_3S_2 and metallic Ni.[31] After hydrogen plasma treatment, the XRD pattern of *p*-Rh/Fe-Ni_3S_2/NF shows characteristic peaks of both Ni_3S_2 and Rh_2S_3 phases. Meanwhile, a new peak at 41° from metallic Rh (PDF no. 05-0685) appears, suggesting Rh formation under reductive hydrogen plasma. The weak characteristic peaks of the Rh_2S_3 phase suggest a low loading of Rh on the nanosheets and low Rh_2S_3 crystallinity.

In the Raman spectra in Fig. 1c, Fe-Ni_3S_2 shows several peaks in the 260–380 cm^{-1} range from the vibration of the Ni(Fe)–S bond. The broad peaks at around 530 cm^{-1} can be attributed to the Ni^{2+}–O vibration formed on the surface of Fe-Ni_3S_2/NF in the air.[32] After Rh incorporation, the Raman spectrum of Rh/Fe-Ni_3S_2/NF displays two additional peaks at 199 and 220 cm^{-1}, indicating the formation of a Rh–S bond, consistent with its XRD pattern in Fig. 1b.[33] After hydrogen plasma treatment, the peaks in the low wavenumber region were considerably weakened for *p*-Rh/Fe-Ni_3S_2/NF, indicating the partial damage of M–S (M = Rh, Ni and Fe) bonds due to the strong etching effect and reducing ability of hydrogen plasma; meanwhile a broad peak arises at around 500 cm^{-1}, implying the reduction of surface oxide species. During this process, partial surface S atoms were removed by active H radicals and abundant S vacancies were formed on the nanosheets, accompanied by the reduction of metal atoms and the decrease of sulfide crystallinity, in accordance with the XRD results in Fig. 1b.[34]

The TEM image in Fig. 2a shows an individual *p*-Rh/Fe-Ni_3S_2 nanosheet with a lateral dimension of hundreds of nanometers. There are rich clusters embedded in the nanosheet. The diameter of most clusters is between 2.0 and 5.0 nm according to the statistical size distribution (inset in Fig. 2a). The high-resolution TEM images in Fig. 2b and c show several crystalline domains with clear lattice fringes for the clusters in the *p*-Rh/Fe-Ni_3S_2 nanosheet. Two crystalline domains assigned to metallic Rh and Rh_2S_3 are shown in Fig. 2b with clear Rh/Rh_2S_3 interfaces. In Fig. 2c, the clear lattice fringes could be assigned to Ni_3S_2 and Rh_2S_3, respectively. Meanwhile, some regions as indicated with white circles in Fig. 2b and c

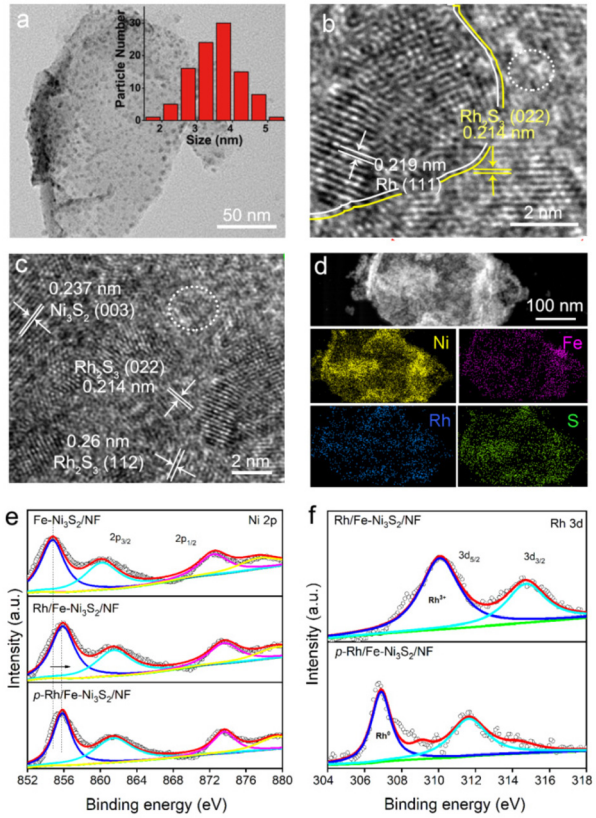

Fig. 2 TEM images (a, b, c) and elemental mapping images (d) of *p*-Rh/Fe-Ni_3S_2/NF; inset in (a) shows the size distribution of the nanoclusters; XPS Ni 2p (e) and Rh 3d spectra of *p*-Rh/Fe-Ni_3S_2/NF and other catalysts.

on the nanosheet show no clear lattice pattern, manifesting the amorphous nature of these areas as a result of hydrogen plasma treatment. The selected area electron diffraction (SAED) pattern in Fig. S2† shows three distinct diffraction rings from Ni_3S_2 (PDF44-1418), Rh_2S_3 (PDF35-0736), and metallic Rh (PDF05-0685), further verifying the hybrid compositions of the *p*-Rh/Fe-Ni_3S_2 nanosheets. Besides, the corresponding EDX mapping images (Fig. 2d) of an individual *p*-Rh/Fe-Ni_3S_2/NF nanosheet display that Ni, Fe, Rh, and S elements are distributed on the *p*-Rh/Fe-Ni_3S_2 nanosheets.

The Ni 2p XPS spectrum of Fe-Ni_3S_2/NF (Fig. 2e) shows two peaks at 872.3 and 854.8 eV, each with a satellite peak that can be assigned to Ni $2p_{1/2}$ and Ni $2p_{3/2}$, respectively.[13,35] After Rh incorporation, the binding energy of Ni 2p in Rh/Fe-Ni_3S_2/NF is considerably increased, indicative of the electronic interaction between Ni and Rh. In the Rh 3d spectrum of Rh/Fe-Ni_3S_2/NF (Fig. 2f), two peaks at 309.9 and 314.5 eV are well assigned to Rh $3d_{5/2}$ and $3d_{3/2}$. Both peaks of Rh 3d in *p*-Rh/Fe-Ni_3S_2/NF are negatively shifted after hydrogen plasma treatment, suggesting the reduction of Rh^{3+} to Rh (0).[13,36,37] The binding energy of Ni 2p remains unchanged after plasma treatment, which may be due to the fact that Rh is easier to be reduced than Ni and plasma reduced metallic Ni, if any, is apt to be re-oxidized after exposure to air. For S 2p, the peak intensity at 168.2 eV from the oxidized S species on *p*-Rh/Fe-Ni_3S_2/NF is considerably decreased compared to Fe-Ni_3S_2/NF and Rh/Fe-Ni_3S_2/NF (Fig. S3†), indicating the reduction of SO_x species by hydrogen plasma, in line with the Raman spectra in Fig. 1c. For Fe 2p spectra, no evident difference is observed among *p*-Rh/Fe-Ni_3S_2/NF, Fe-Ni_3S_2/NF, and Rh/Fe-Ni_3S_2/NF (Fig. S4†).

3.2. OER performance of *p*-Rh/Fe-Ni_3S_2/NF

The OER performance of *p*-Rh/Fe-Ni_3S_2/NF was evaluated in 1.0 M KOH. As shown in Fig. 3a, all the catalysts show an anodic peak at ~1.32 V on linear scan voltammetry (LSV) curves due to the nominal oxidation of Ni^{2+} to Ni^{3+}, followed by a sharply increased anodic OER current with a further polarized potential. *p*-Rh/Fe-Ni_3S_2/NF clearly shows advantageous OER activity over Fe-Ni_3S_2/NF, Rh/Fe-Ni_3S_2/NF, and RuO_2/NF. To achieve 100, 200, and 300 mA cm^{-2} current, *p*-Rh/Fe-Ni_3S_2/NF needs overpotentials of 237, 251, and 259 mV, much lower than those of Fe-Ni_3S_2/NF, Rh/Fe-Ni_3S_2/NF, and RuO_2/NF, respectively (Fig. 3b). The Tafel slopes of all catalysts were calculated and are presented in Fig. 3c, showing the lowest Tafel slope of 49 mV dec^{-1} of *p*-Rh/Fe-Ni_3S_2/NF, indicating its favorable OER kinetics over its rivals. In EIS collected at 1.524 V shown in Fig. 3d, *p*-Rh/Fe-Ni_3S_2/NF possesses a smaller charge transfer resistance (R_{ct}) than its two analogues,

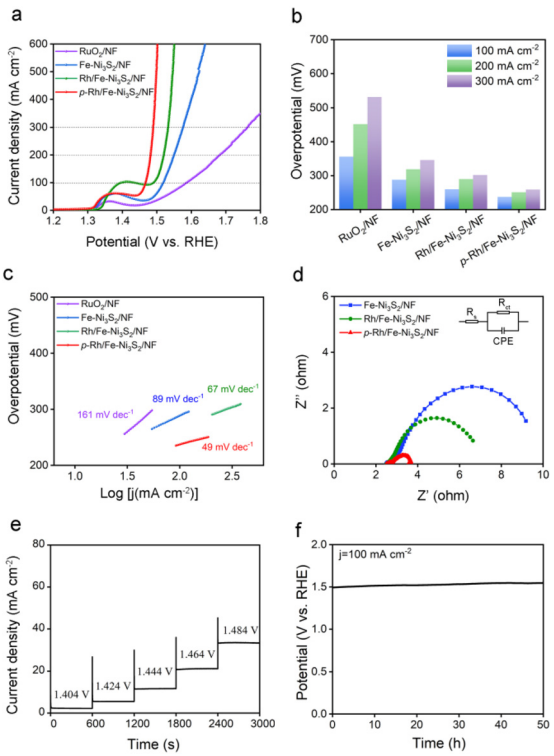

Fig. 3 OER performance of *p*-Rh/Fe-Ni_3S_2/NF in 1 M KOH. (a) *iR*-compensated polarization curves at 5 mV s^{-1}, (b) overpotentials required at a given current density, (c) Tafel plots, (d) Nyquist plots of various catalysts collected at 1.524 V with the corresponding equivalent circuit, (e) multi-step chronoamperometric curve (without *iR* correction), and (f) chronopotentiometric curve of *p*-Rh/Fe-Ni_3S_2/NF at 100 mA cm^{-2}.

indicating faster OER kinetics. This comparison clearly demonstrates that Rh-incorporation in Fe-Ni_3S_2/NF efficiently enhances the OER performance of the resultant Rh/Fe-Ni_3S_2/NF, and subsequent hydrogen plasma treatment further promotes the catalytic activity.

To differentiate the current from the OER and oxidation of Ni^{2+}, a multi-step chronoamperometric measurement was carried out. As shown in Fig. 3e, when the potential of the *p*-Rh/Fe-Ni_3S_2/NF electrode was held at 1.404 V, nearly constant anodic current was observed on the electrode for 600 s. Stepping to 1.424 V and higher results in a prompt increase in the anodic current, verifying that the observed anodic current is indeed from the OER but not from possible oxidation of surface metal species as the latter cannot afford such high and continuous currents. Chronopotentiometric measurement in Fig. 3f further highlights the excellent durability of *p*-Rh/Fe-Ni_3S_2/NF. The potential increases slightly from 1.49 V to 1.54 V during 50 h of uninterrupted electrolysis at a constant current density of 100 mA cm^{-2}.

3.3. Mechanism of enhanced OER activity of *p*-Rh/Fe-Ni_3S_2/NF

To investigate the intrinsic OER activity of *p*-Rh/Fe-Ni_3S_2/NF, the electrochemical surface areas (ECSAs) of these catalysts were measured by the double-layer capacitance (C_{dl}) method. As shown in Fig. S5,† *p*-Rh/Fe-Ni_3S_2/NF exhibits the highest C_{dl} (25.53 mF cm^{-2}) compared to those of Rh/Fe-Ni_3S_2/NF and Fe-Ni_3S_2/NF, suggesting an increase in the active area of *p*-Rh/Fe-Ni_3S_2/NF to promote its OER performance.[38] Remarkably, the intrinsic OER activity of *p*-Rh/Fe-Ni_3S_2/NF is still higher than its two rivals after ECSA-normalization (Fig. S6†), manifesting that its high OER performance is associated not only with its high surface areas but also with its promoted intrinsic activity.

Post-OER characterization was carried out to investigate the possible mechanism of the enhanced intrinsic activity of *p*-Rh/Fe-Ni_3S_2/NF. From the SEM image in Fig. S7,† the *p*-Rh/Fe-Ni_3S_2/NF nanosheets become clumpy nanoparticles after the long-term OER, indicating dramatic reconstruction of the nanostructure during the harsh OER process. The Rh content in the catalyst remains almost unchanged (~42 μg cm^{-2}) after the long-term OER, as measured by ICP-AES, indicating negligible Rh dissolution. The XRD pattern in Fig. 4a proves that after the long-term OER, *p*-Rh/Fe-Ni_3S_2/NF exhibits newly-appeared peaks of NiOOH and Rh_2O_3 (PDF no. 41-0541). The characteristic peaks of Ni_3S_2 remain but those from metallic Rh and Rh_2S_3 disappear. The Rh 3d XPS spectrum of *p*-Rh/Fe-Ni_3S_2/NF after the OER demonstrates positively shifted binding energy (Fig. S8†), again suggesting the formation of the Rh_2O_3 phase from metallic Rh and Rh_2S_3 after the OER process. The TEM image in Fig. S9† also shows that the pristine nanosheet morphology was partly destroyed, and some nanoparticles were retained on the nanosheets to form agglomerations, in good agreement with SEM in Fig. S7.† The high-resolution TEM image in Fig. 4b displays clear lattice fringes with inter-planar distances corresponding to the NiOOH (101), Rh_2O_3 (202) and Ni_3S_2 (110) planes, respectively.

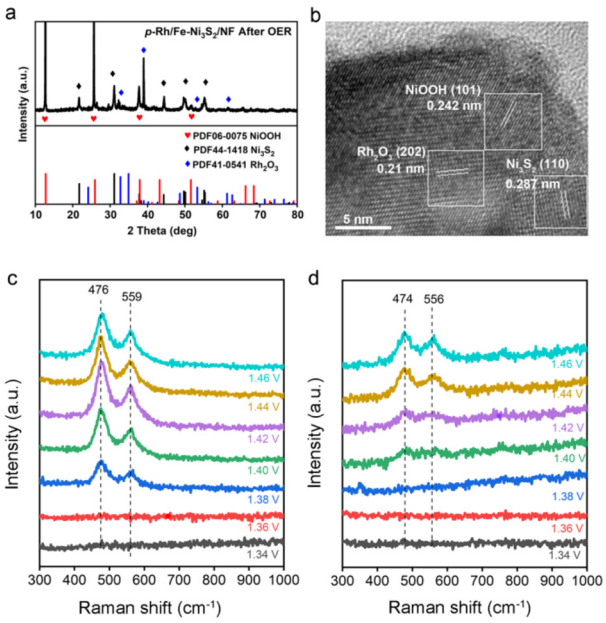

Fig. 4 Post-OER characterization of *p*-Rh/Fe-Ni_3S_2/NF after 50 h of the OER at 100 mA cm^{-2}: (a) XRD pattern and (b) TEM images. (c and d) OER *in situ* Raman spectra of (c) *p*-Rh/Fe-Ni_3S_2/NF and (d) Fe-Ni_3S_2/NF at different polarized potentials.

The SAED pattern confirms the same crystalline compositions of *p*-Rh/Fe-Ni_3S_2/NF after the OER (Fig. S10†). These post-OER characterization studies unambiguously suggest that *p*-Rh/Fe-Ni_3S_2/NF experiences surface transformation and nanostructure reconstruction during the long-term OER; NiOOH and Rh_2O_3 are *in situ* formed on *p*-Rh/Fe-Ni_3S_2/NF during the OER;[8,10] meanwhile, the partial Ni_3S_2 phase survives to support the catalytically active phase in the OER.

In situ Raman spectroscopy was used to investigate the surface reconstruction of *p*-Rh/Fe-Ni_3S_2/NF under OER *operando* conditions. As shown in Fig. 4c, there are two obvious peaks at 476 and 559 cm^{-1} on *p*-Rh/Fe-Ni_3S_2/NF at 1.38 V and higher, corresponding to two vibration modes (e_g bending and A_{1g} stretching) of the Ni^{3+}–O bond, both of which indicate the formation of the NiOOH phase at the anodic potential.[2,8,39] The Fe-Ni_3S_2/NF catalyst also exhibits similar potential-dependent Raman spectra, as in Fig. 4d. Notably, the e_g and A_{1g} wavenumbers of *p*-Rh/Fe-Ni_3S_2/NF are shifted to higher values compared to Fe-Ni_3S_2/NF, which implies that the Ni^{3+}–O bond in *p*-Rh/Fe-Ni_3S_2/NF was compressed to possess a shorter bond length.[40] The NiOOH formation starts at 1.38 V for *p*-Rh/Fe-Ni_3S_2/NF, which is earlier than that of Fe-Ni_3S_2/NF (1.42 V), manifesting that the Rh incorporation is beneficial for Ni oxidation, which is able to promote the OER process.[41] The intensity ratio between the A_{1g} peak (~560 cm^{-1}) and the e_g peak (~475 cm^{-1}) of *p*-Rh/Fe-Ni_3S_2/NF at 1.46 V reaches 0.64, which is considerably lower than that of Fe-Ni_3S_2/NF (0.77) at the same potential, indicating the higher order level of NiOOH.[8,40] Previous work has revealed that too many Fe dopants in NiOOH result in a higher disorder level and impair the OER activity.[8,40] In the present work, it is believed that Rh atoms

are doped into the NiOOH matrix to form di-μ-oxo bridged Ni–O–Rh sites while keeping the NiOOH with a high order level to enhance the OER activity. The Rh atom possesses higher electron affinity compared to Fe and Ni atoms, resulting in a shorter and stronger Ni–O bond in Ni–O–Rh and a lower oxidative potential for the conversion of Ni^{2+} to Ni^{3+}. The formed Ni–O–Rh sites together with the Ni–O–Fe sites contribute to the OER activity of *p*-Rh/Fe-Ni_3S_2/NF. Without hydrogen plasma, such active sites cannot be formed efficiently, and that is the case for Rh/Fe-Ni_3S_2/NF.

DFT calculations were performed to rationalize the enhanced OER activity of *p*-Rh/Fe-Ni_3S_2/NF. Rh/Fe-doped NiOOH was employed to model the OER process in contrast to Fe-doped NiOOH. The optimal surfaces on two catalysts were first calculated and determined, respectively, as shown in Fig. 5a and b. A conventional four-step mechanism (*OH, *O, and *OOH; * denotes the active site) was adopted to describe the OER process.[42,43] For Fe-doped NiOOH without Rh, the process of *OH to *O is the rate determining step of the OER (Fig. 5c), and the overpotential is calculated to be 0.71 eV, which is lower than that of the pure NiOOH surface (Fig. S11†), suggesting a tremendous improvement of Fe-doping on the OER activity. With Rh incorporated, the rate determining step remains unchanged but the overpotential required further decreases to 0.63 eV (Fig. 5d), indicating that Rh-doping strengthens the binding of *O to facilitate the rate determining step and accelerates the whole OER process.

3.4. HER performance of *p*-Rh/Fe-Ni_3S_2/NF

p-Rh/Fe-Ni_3S_2/NF shows excellent HER activity in alkaline solution as well. As depicted in Fig. 6a, Fe-Ni_3S_2/NF requires an overpotential of 191 mV to achieve an HER current of 10 mA cm^{-2}, indicating its limited HER activity. After Rh incorporation, the overpotential of Rh/Fe-Ni_3S_2/NF largely decreases to 91 mV at the same current density. *p*-Rh/Fe-Ni_3S_2/NF itself, in sharp contrast, needs overpotentials of only 25 and 108 mV to achieve HER current values of 10 and 100 mA cm^{-2}, respectively (Fig. 6b). Although still inferior to the benchmark Pt/C catalyst, it significantly outperforms those of Fe-Ni_3S_2/NF and Rh/Fe-Ni_3S_2/NF, indicating the important role of Rh incorporation and hydrogen plasma treatment. The Tafel slope of the *p*-Rh/Fe-Ni_3S_2/NF was found to be 66 mV dec^{-1}, which is smaller than that of Rh/Fe-Ni_3S_2/NF and Fe-Ni_3S_2/NF, as shown in Fig. 6c, indicating the fast HER kinetics of *p*-Rh/Fe-Ni_3S_2/NF. The EIS spectrum of *p*-Rh/Fe-Ni_3S_2/NF in Fig. 6d shows a smaller charge transfer resistance than those of Rh/Fe-Ni_3S_2/NF and Fe-Ni_3S_2/NF due to the promotion effect of Rh-doping and plasma treatment on HER activity. Meanwhile, during 50 h of HER operation at a constant current of 100 mA cm^{-2}, the overpotential of *p*-Rh/Fe-Ni_3S_2/NF slightly increases by 49 mV (Fig. 6e). The polarization curve of *p*-Rh/Fe-Ni_3S_2/NF after a 1000-cycle accelerated stability test completely overlaps with that of the pristine one (Fig. 6f), again implying its excellent HER durability.

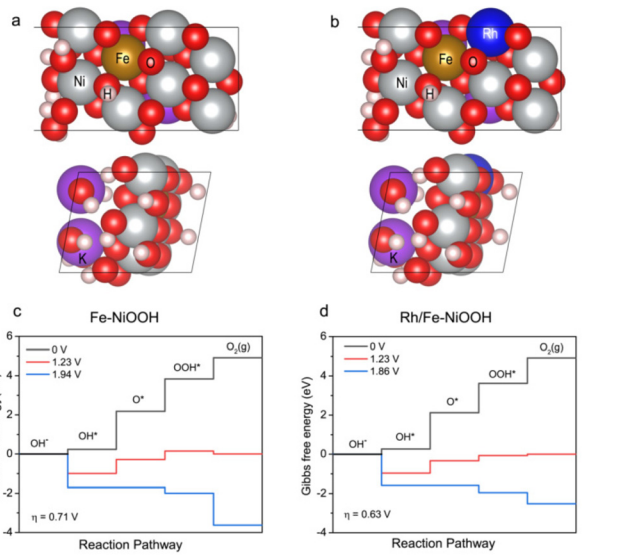

Fig. 5 DFT calculation of the OER process on Fe-doped NiOOH and Rh/Fe-doped NiOOH surfaces. Side (upper) and top views (bottom) of the model surfaces of Fe-doped NiOOH (a) and Rh/Fe-doped NiOOH (b); free energy diagrams of the OER on Fe-doped NiOOH (c) and Rh/Fe-doped NiOOH (d).

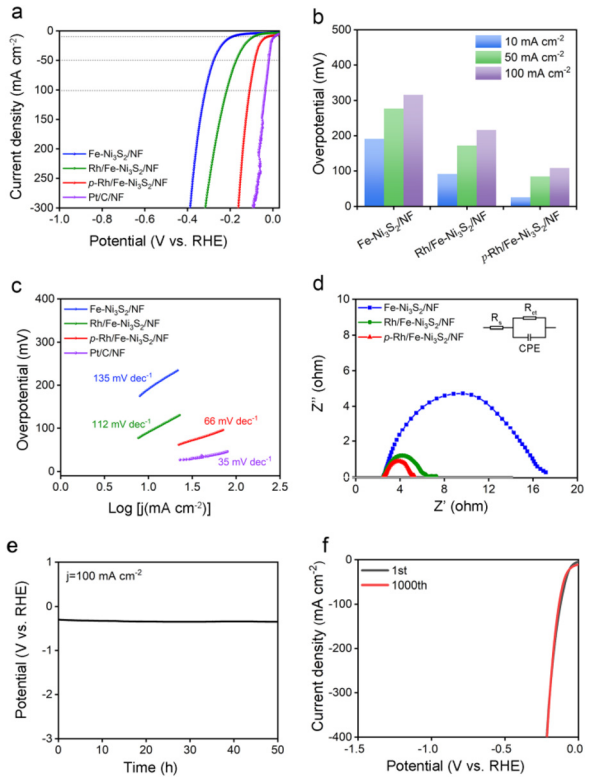

Fig. 6 HER performance of *p*-Rh/Fe-Ni_3S_2/NF in comparison to other catalysts in 1 M KOH. (a) *iR*-corrected polarization curves at 5 mV s^{-1}, (b) overpotentials required at a given current density, (c) Tafel plots, (d) Nyquist plots of various catalysts collected at −0.296 V with an equivalent circuit, (e) chronopotentiometry curve at 100 mA cm^{-2}, and (f) LSV curves of *p*-Rh/Fe-Ni_3S_2/NF before and after 1000 cycles of CV, scanning rate: 5 mV s^{-1}.

3.5. Mechanism of enhanced HER activity of *p*-Rh/Fe-Ni_3S_2/NF

As shown in Fig. S12,† *p*-Rh/Fe-Ni_3S_2/NF displays a higher ECSA than Rh/Fe-Ni_3S_2/NF and Fe-Ni_3S_2/NF upon an HER test, suggesting that Rh incorporation and subsequent hydrogen plasma treatment introduce abundant defects and vacancies in the nanosheets.[44] ECSA-normalized LSV curves in Fig. S13† further confirm that the intrinsic HER activity of *p*-Rh/Fe-Ni_3S_2/NF is also improved compared to Rh/Fe-Ni_3S_2/NF and Fe-Ni_3S_2/NF. The XRD pattern (Fig. S14†) shows that all the diffraction peaks of *p*-Rh/Fe-Ni_3S_2/NF remain after HER catalysis; no new crystalline phase was detected. At the same time, it maintains a nanosheet morphology after the long-term HER according to the SEM image in Fig. S15.† In XPS spectra (Fig. S16†), no obvious shift in the binding energy of Ni 2p, Rh 3d, Fe 2p and S 2p was observed for *p*-Rh/Fe-Ni_3S_2/NF after long-term HER catalysis. The Rh content in the catalyst slightly decreases to ~34 μg cm^{-2} after 50 h of the HER, indicating mild Rh leakage. Therefore, *p*-Rh/Fe-Ni_3S_2/NF preserves its compositional and structural properties during the HER, which is in sharp contrast with the situation for the OER.

Rh_2S_3 has been reported to be highly active for the HER and hydrogen oxidation reaction (HOR).[25,33] Meanwhile, metallic Rh supported on various substrates such as Si, SWCNTs, MoS_2, *etc.* in the form of clusters, nanoparticles or single atoms demonstrates excellent HER activity.[37,45,46] In the present work the enhanced HER activity of *p*-Rh/Fe-Ni_3S_2/NF over Rh/Fe-Ni_3S_2/NF and Fe-Ni_3S_2/NF suggests that the co-existence of metallic Rh and Rh_2S_3 is critical for the HER activity. Therefore, the Rh/Rh_2S_3 heterostructure may be responsible for the HER activity due to its optimal hydrogen adsorption strength.

DFT calculation was carried out to verify this synergistic effect between Rh and Rh_2S_3. The optimal structural model of the Rh_2S_3/Rh interface was first determined by considering the lattice matching of Rh and Rh_2S_3 planes, as shown in Fig. 7a (model surfaces of pure Rh and pure Rh_2S_3 shown in Fig. S17†). At such a heterointerface, the water adsorption energy was first calculated as it is important to initiate the HER in an alkaline environment.[47] As in Fig. 7b, the H_2O adsorption energies on the Rh part, Rh_2S_3 part and interface of the Rh_2S_3/Rh heterojunction are −0.570, −0.592, and −0.659 eV, respectively; all are higher than those of pure Rh_2S_3 (−0.544 eV) and Rh (−0.447 eV), suggesting stronger H_2O adsorption energy, which is capable of speeding up the HER process.[48] The hydrogen adsorption energy (ΔG_{H^*}) on the model surface was further calculated (Fig. 7c). The ΔG_{H^*} on the interface of the Rh_2S_3/Rh heterojunction is ~−0.05 eV, which is smaller than that on the Rh surface (−0.185 eV) and the Rh_2S_3 part (0.476 eV) of the Rh_2S_3/Rh heterojunction, and is also lower than that on pure Rh_2S_3 (0.540 eV) and Rh (−0.272 eV). This result indicates that the most active site is the Rh–Rh_2S_3 interface, where the favorable H* adsorption energy leads to excellent HER activity. Notably, the charge density differential image reveals that a strong interaction occurred at the interface of Rh_2S_3/Rh (Fig. S18†), leading to lattice distortion and electron rearrangement of Rh_2S_3 and Rh, and improving their HER activity compared to their corresponding pure phases.

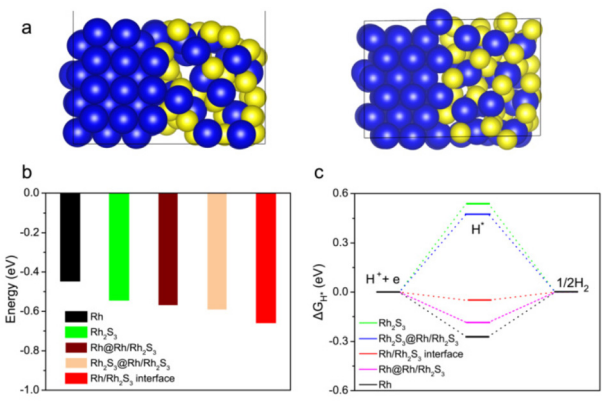

Fig. 7 DFT calculation of the HER process on *p*-Rh/Fe-Ni_3S_2/NF. (a) Side (left) and top view (right) of the model surface used for the Rh_2S_3/Rh heterointerface. Blue and yellow balls represent Rh and S atoms, respectively; calculated water adsorption energies (b) and ΔG_{H^*} (c) on Rh_2S_3/Rh, Rh_2S_3 and Rh.

3.6. Influence of H_2 plasma treatment

To further clarify the effect of H_2 plasma treatment on the synthesis of *p*-Rh/Fe-Ni_3S_2/NF, thermal treatment of Rh/Fe-Ni_3S_2 was carried out in a H_2/Ar atmosphere at 350 °C to obtain the catalyst of Rh/Fe-Ni_3S_2-350. The XRD pattern indicates the same crystal phases (metallic Rh, Rh_2S_3, and Ni_3S_2) of as-produced Rh/Fe-Ni_3S_2-350 as *p*-Rh/Fe-Ni_3S_2/NF, suggesting the partial reduction of Rh_2S_3 to metallic Rh after thermal treatment (Fig. S19†). However, the Rh/Fe-Ni_3S_2-350 is inferior to the *p*-Rh/Fe-Ni_3S_2/NF in terms of HER and OER activity (Fig. S20†), even though both catalysts are composed of the same components. This comparison implies that plasma treatment for the synthesis of *p*-Rh/Fe-Ni_3S_2/NF is necessary and cannot be displaced by thermal annealing in H_2. Meanwhile, the duration of H_2 plasma treatment was also investigated and an optimal duration of 20 min was found, at which the resultant *p*-Rh/Fe-Ni_3S_2/NF exhibits the best HER and OER performance (Fig. S21†). Ar plasma was also investigated but it cannot afford the same enhancement effect on OER or HER activity as hydrogen plasma (Fig. S22†). These observations indicate that H_2 plasma treatment is used not only to simply reduce some sulfides to metal, but also results in rich surface defects and nanostructure reconstruction to facilitate electrocatalysis; there is a balance between the etching/reducing effects of plasma treatment to maximize the electrocatalytic activity of this catalyst.

3.7. Overall water splitting of *p*-Rh/Fe-Ni_3S_2/NF

Electrochemical evaluations suggest that *p*-Rh/Fe-Ni_3S_2/NF is a highly active HER/OER bifunctional electrocatalyst even though its real active phase is different under two electrochemical environments. As shown in Fig. 8a, *p*-Rh/Fe-Ni_3S_2/NF

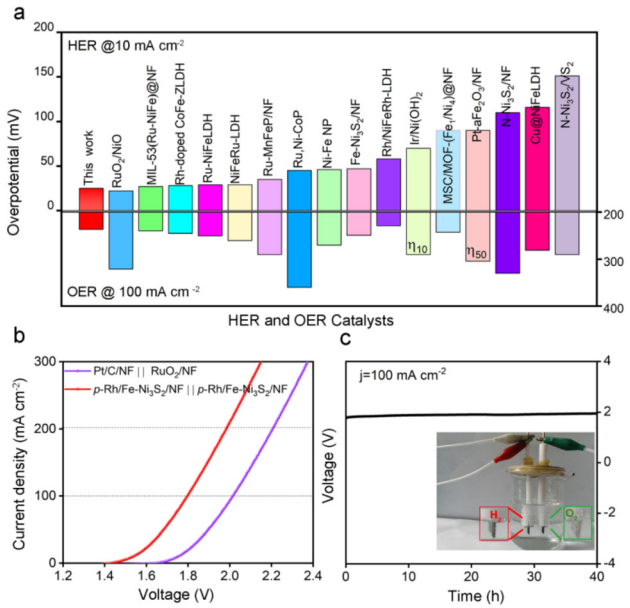

Fig. 8 Performance comparison of *p*-Rh/Fe-Ni_3S_2/NF and other bifunctional catalysts. (a) Overpotential at a current density of 10 mA cm^{-2} for the HER and 100 mA cm^{-2} for the OER, respectively. (b) polarization curves (without *iR*-compensation) of the *p*-Rh/Fe-Ni_3S_2/NF||*p*-Rh/Fe-Ni_3S_2/NF and Pt/C/NF||RuO_2 /NF alkaline water electrolyzer at 5 mV s^{-1}; (c) chronopotentiometric curve of *p*-Rh/Fe-Ni_3S_2/NF||*p*-Rh/Fe-Ni_3S_2/NF at 100 mA cm^{-2} without *iR*-compensation. The inset in (c) shows the optical image of this electrolyzer under operation.

was among the best HER/OER bifunctional catalysts reported in the literature.[10,16,22,49–62]

Due to its good OER/HER activity, *p*-Rh/Fe-Ni_3S_2/NF was employed to assemble an alkaline electrolyzer as both an anodic and a cathodic catalyst. As shown in Fig. 8b, the as-assembled electrolyzer achieves higher electrolytic current than the one with commercial Pt/C and RuO_2 on NF as cathodic and anodic catalysts at the same cell voltage. It needs a low cell voltage of 1.79 V to obtain an electrolytic current of 100 mA cm^{-2}, while the precious-metal based one needs 2.0 V to achieve the same current, unambiguously confirming the high activity of *p*-Rh/Fe-Ni_3S_2/NF. Meanwhile, this electrolyzer is able to stably operate at 100 mA cm^{-2} for 40 h (Fig. 8c), showing excellent catalytic stability of *p*-Rh/Fe-Ni_3S_2/NF as the bifunctional catalyst. The faradaic efficiency of *p*-Rh/Fe-Ni_3S_2/NF was found to be close to 100% by a drainage method, as shown in Fig. S23.† [63]

4. Conclusions

In summary, we reported *p*-Rh/Fe-Ni_3S_2/NF synthesized *via* wet impregnation and subsequent hydrogen plasma treatment as an excellent HER/OER bifunctional catalyst. By introducing a low content of Rh, the resultant *p*-Rh/Fe-Ni_3S_2/NF exhibits outstanding HER and OER catalytic performance in alkaline media. Remarkably, a unique Janus catalytic mechanism is revealed for *p*-Rh/Fe-Ni_3S_2/NF; it catalyzes the OER and HER with different active phases. For the OER, the doped Rh atoms in the *in situ* formed Ni oxyhydroxide matrix collaborate with the Ni–O–Fe sites to enhance the OER activity; for the HER, the heterostructured Rh/Rh_2S_3 clusters offer active centers while the Ni_3S_2 nanosheets offer high conductivity and large surface areas. Hydrogen plasma was demonstrated to manipulate the compositional and structural properties of a catalyst under mild conditions with broad flexibility and good controllability, thus providing a novel and elegant tool for fabricating efficient catalysts.

Conflicts of interest

There are no conflicts to declare.

Acknowledgements

The financial support from the National Natural Science Foundation of China (No. 22074125), the Natural Science Foundation Project of CQ CSTC (cstc2021jcyj-msxmX1165) and The Innovation Platform for Academicians of Hainan Province is gratefully acknowledged.

References

1 Z. W. Seh, J. Kibsgaard, C. F. Dickens, I. B. Chorkendorff, J. K. Norskov and T. F. Jaramillo, Combining theory and experiment in electrocatalysis: Insights into materials design, *Science*, 2017, **355**, eaad4998.
2 G. Liu, M. Wang, Y. Xu, X. Wang, X. Li, J. Liu, X. Cui and L. Jiang, Porous CoP/Co2P heterostructure for efficient hydrogen evolution and application in magnesium/seawater battery, *J. Power Sources*, 2021, **486**, 229351.
3 Z. Li, X. Dou, Y. Zhao and C. Wu, Enhanced oxygen evolution reaction of metallic nickel phosphide nanosheets by surface modification, *Inorg. Chem. Front.*, 2016, **3**, 1021–1027.
4 R. Gao and D. Yan, Recent Development of Ni/Fe-Based Micro/Nanostructures toward Photo/Electrochemical Water Oxidation, *Adv. Energy Mater.*, 2020, **10**, 1900954.
5 M. Rinawati, Y.-X. Wang, K.-Y. Chen and M.-H. Yeh, Designing a spontaneously deriving NiFe-LDH from bimetallic MOF-74 as an electrocatalyst for oxygen evolution reaction in alkaline solution, *Chem. Eng. J.*, 2021, **423**, 130204.
6 B. S. Yeo and A. T. Bell, In Situ Raman Study of Nickel Oxide and Gold-Supported Nickel Oxide Catalysts for the Electrochemical Evolution of Oxygen, *J. Phys. Chem. C*, 2012, **116**, 8394–8400.
7 J. Du, A. Yu, Z. Zou and C. Xu, One-pot synthesis of iron–nickel–selenide nanorods for efficient and durable electrochemical oxygen evolution, *Inorg. Chem. Front.*, 2018, **5**, 814–818.

8 L. Yi, Y. Niu, B. Feng, M. Zhao and W. Hu, Simultaneous phase transformation and doping via a unique photochemical-electrochemical strategy to achieve a highly active Fe-doped Ni oxyhydroxide oxygen evolution catalyst, *J. Mater. Chem. A*, 2021, **9**, 4213–4220.
9 D. Y. Chung, P. P. Lopes, P. F. B. D. Martins, H. He, T. Kawaguchi, P. Zapol, H. You, D. Tripkovic, D. Strmcnik, Y. Zhu, S. Seifert, S. Lee, V. R. Stamenkovic and N. M. Markovic, Dynamic stability of active sites in hydr (oxy)oxides for the oxygen evolution reaction, *Nat. Energy*, 2020, **5**, 222–230.
10 B. Zhang, C. Zhu, Z. Wu, E. Stavitski, Y. H. Lui, T.-H. Kim, H. Liu, L. Huang, X. Luan, L. Zhou, K. Jiang, W. Huang, S. Hu, H. Wang and J. S. Francisco, Integrating Rh Species with NiFe-Layered Double Hydroxide for Overall Water Splitting, *Nano Lett.*, 2020, **20**, 136–144.
11 W. Jin, H. Wu, W. Cai, B. Jia, M. Batmunkh, Z. Wu and T. Ma, Evolution of interfacial coupling interaction of Ni-Ru species for pH-universal water splitting, *Chem. Eng. J.*, 2021, **426**, 130762.
12 Z. Li, K. Wang, X. Tan, X. Liu, G. Wang, G. Xie and L. Jiang, Defect-enriched multistage skeleton morphology Ni-Fe-P-Ni_3S_2 heterogeneous catalyst on Ni foam for efficient overall water splitting, *Chem. Eng. J.*, 2021, **424**, 130390.
13 H. Sun, W. Zhang, J.-G. Li, Z. Li, X. Ao, K.-H. Xue, K. K. Ostrikov, J. Tang and C. Wang, Rh-engineered ultrathin NiFe-LDH nanosheets enable highly-efficient overall water splitting and urea electrolysis, *Appl. Catal., B*, 2021, **284**, 119740.
14 K. Wang, B. Li, J. Ren, W. Chen, J. Cui, W. Wei and P. Qu, Ru@Ni_3S_2 nanorod arrays as highly efficient electrocatalysts for the alkaline hydrogen evolution reaction, *Inorg. Chem. Front.*, 2022, **9**, 3885.
15 Q. Wang, X. Huang, Z. L. Zhao, M. Wang, B. Xiang, J. Li, Z. Feng, H. Xu and M. Gu, Ultrahigh-Loading of Ir Single Atoms on NiO Matrix to Dramatically Enhance Oxygen Evolution Reaction, *J. Am. Chem. Soc.*, 2020, **142**, 7425–7433.
16 G. Zhao, P. Li, N. Cheng, S. X. Dou and W. Sun, An Ir/$Ni(OH)_2$ Heterostructured Electrocatalyst for the Oxygen Evolution Reaction: Breaking the Scaling Relation, Stabilizing Iridium(v), and Beyond, *Adv. Mater.*, 2020, **32**, 2000872.
17 P. Su, W. Pei, X. Wang, Y. Ma, Q. Jiang, J. Liang, S. Zhou, J. Zhao, J. Liu and G. Q. Lu, Exceptional Electrochemical HER Performance with Enhanced Electron Transfer between Ru Nanoparticles and Single Atoms Dispersed on a Carbon Substrate, *Angew. Chem., Int. Ed.*, 2021, **60**, 16044.
18 Y. Sun, Z. Xue, Q. Liu, Y. Jia, Y. Li, K. Liu, Y. Lin, M. Liu, G. Li and C.-Y. Su, Modulating electronic structure of metal-organic frameworks by introducing atomically dispersed Ru for efficient hydrogen evolution, *Nat. Commun.*, 2021, **12**, 1369.
19 L.-L. Feng, G. Yu, Y. Wu, G.-D. Li, H. Li, Y. Sun, T. Asefa, W. Chen and X. Zou, High-Index Faceted Ni_3S_2 Nanosheet Arrays as Highly Active and Ultrastable Electrocatalysts for Water Splitting, *J. Am. Chem. Soc.*, 2015, **137**, 14023.
20 X. Zou, Y. Liu, G.-D. Li, Y. Wu, D.-P. Liu, W. Li, H.-W. Li, D. Wang, Y. Zhang and X. Zou, Ultrafast Formation of Amorphous Bimetallic Hydroxide Films on 3D Conductive Sulfide Nanoarrays for Large-Current-Density Oxygen Evolution Electrocatalysis, *Adv. Mater.*, 2017, **29**, 1700404.
21 Y. Wu, Y. Li, M. Yuan, H. Hao, X. San, Z. Lv, L. Xu and B. Wei, Operando capturing of surface self-reconstruction of Ni3S2/FeNi2S4 hybrid nanosheet array for overall water splitting, *Chem. Eng. J.*, 2022, **427**, 131944.
22 J. Liu, Y. Zheng, Y. Jiao, Z. Wang, Z. Lu, A. Vasileff and S.-Z. Qiao, NiO as a Bifunctional Promoter for RuO_2 toward Superior Overall Water Splitting, *Small*, 2018, **14**, 1704073.
23 C. C. L. McCrory, S. Jung, J. C. Peters and T. F. Jaramillo, Benchmarking Heterogeneous Electrocatalysts for the Oxygen Evolution Reaction, *J. Am. Chem. Soc.*, 2013, **135**, 16977.
24 G. Zhou, M. Li, Y. Li, H. Dong, D. Sun, X. Liu, L. Xu, Z. Tian and Y. Tang, Regulating the Electronic Structure of CoP Nanosheets by O Incorporation for High-Efficiency Electrochemical Overall Water Splitting, *Adv. Funct. Mater.*, 2020, **30**, 1905252.
25 D. Yoon, B. Seo, J. Lee, K. S. Nam, B. Kim, S. Park, H. Baik, S. H. Joo and K. Lee, Facet-controlled hollow Rh_2S_3 hexagonal nanoprisms as highly active and structurally robust catalysts toward hydrogen evolution reaction, *Energy Environ. Sci.*, 2016, **9**, 850.
26 Y. Xu, H. Lv, H. Lu, Q. Quan, W. Li, X. Cui, G. Liu and L. Jiang, Mg/seawater batteries driven self-powered direct seawater electrolysis systems for hydrogen production, *Nano Energy*, 2022, **98**, 107295.
27 W. Li, D. Wang, Y. Zhang, L. Tao, T. Wang, Y. Zou, Y. Wang, R. Chen and S. Wang, Defect Engineering for Fuel-Cell Electrocatalysts, *Adv. Mater.*, 2020, **32**, 1907879.
28 L. Zeng, K. Sun, X. Wang, Y. Liu, Y. Pan, Z. Liu, D. Cao, Y. Song, S. Liu and C. Liu, Three-dimensional-networked Ni_2P/Ni_3S_2 heteronanoflake arrays for highly enhanced electrochemical overall-water-splitting activity, *Nano Energy*, 2018, **51**, 26.
29 Y. Wu, G.-D. Li, Y. Liu, L. Yang, X. Lian, T. Asefa and X. Zou, Overall Water Splitting Catalyzed Efficiently by an Ultrathin Nanosheet-Built, Hollow Ni_3S_2-Based Electrocatalyst, *Adv. Funct. Mater.*, 2016, **26**, 4839.
30 T. Ling, D.-Y. Yan, H. Wang, Y. Jiao, Z. Hu, Y. Zheng, L. Zheng, J. Mao, H. Liu, X.-W. Du, M. Jaroniec and S.-Z. Qiao, Activating cobalt(II) oxide nanorods for efficient electrocatalysis by strain engineering, *Nat. Commun.*, 2017, **8**, 1509.
31 N. Singh, M. Gordon, H. Metiu and E. McFarland, Doped rhodium sulfide and thiospinels hydrogen evolution and oxidation electrocatalysts in strong acid electrolytes, *J. Appl. Electrochem.*, 2016, **46**, 497.
32 C. Hu, Y. Hu, C. Fan, L. Yang, Y. Zhang, H. Li and W. Xie, Surface-Enhanced Raman Spectroscopic Evidence of Key Intermediate Species and Role of NiFe Dual-Catalytic

Center in Water Oxidation, *Angew. Chem., Int. Ed.*, 2021, **60**, 19774.
33 N. Singh, J. Hiller, H. Metiu and E. McFarland, Investigation of the Electrocatalytic Activity of Rhodium Sulfide for Hydrogen Evolution and Hydrogen Oxidation, *Electrochim. Acta*, 2014, **145**, 224.
34 C. Yang, Z. Wang, T. Lin, H. Yin, X. Lu, D. Wan, T. Xu, C. Zheng, J. Lin, F. Huang, X. Xie and M. Jiang, Core-Shell Nanostructured "Black" Rutile Titania as Excellent Catalyst for Hydrogen Production Enhanced by Sulfur Doping, *J. Am. Chem. Soc.*, 2013, **135**, 17831.
35 D. Khang Ngoc, P. Zheng, Z. Dai, Y. Zhang, R. Dangol, Y. Zheng, B. Li, Y. Zong and Q. Yan, Ultrathin Porous NiFeV Ternary Layer Hydroxide Nanosheets as a Highly Efficient Bifunctional Electrocatalyst for Overall Water Splitting, *Small*, 2018, **14**, 1703257.
36 G. Ma, Q. Xue, J. Zhu, X. Zhang, X. Wang, H. Yao, G. Zhou and Y. Chen, Ultrafine Rh nanocrystals decorated ultrathin NiO nanosheets for urea electro-oxidation, *Appl. Catal., B*, 2020, **265**, 118567.
37 X. Meng, C. Ma, L. Jiang, R. Si, X. Meng, Y. Tu, L. Yu, X. Bao and D. Deng, Distance Synergy of MoS_2-Confined Rhodium Atoms for Highly Efficient Hydrogen Evolution, *Angew. Chem., Int. Ed.*, 2020, **59**, 10502.
38 S. Anantharaj, S. R. Ede, K. Karthick, S. S. Sankar, K. Sangeetha, P. E. Karthik and S. Kundu, Precision and correctness in the evaluation of electrocatalytic water splitting: revisiting activity parameters with a critical assessment, *Energy Environ. Sci.*, 2018, **11**, 744.
39 M. W. Louie and A. T. Bell, An Investigation of Thin-Film Ni-Fe Oxide Catalysts for the Electrochemical Evolution of Oxygen, *J. Am. Chem. Soc.*, 2013, **135**, 12329.
40 S. Lee, K. Banjac, M. Lingenfelder and X. Hu, Oxygen Isotope Labeling Experiments Reveal Different Reaction Sites for the Oxygen Evolution Reaction on Nickel and Nickel Iron Oxides, *Angew. Chem., Int. Ed.*, 2019, **58**, 10295.
41 S. Shi and D. Qin, Bifunctional Metal Nanocrystals for Catalyzing and Reporting on Chemical Reactions, *Angew. Chem., Int. Ed.*, 2020, **59**, 3782.
42 I. C. Man, H.-Y. Su, F. Calle-Vallejo, H. A. Hansen, J. I. Martinez, N. G. Inoglu, J. Kitchin, T. F. Jaramillo, J. K. Norskov and J. Rossmeisl, Universality in Oxygen Evolution Electrocatalysis on Oxide Surfaces, *ChemCatChem*, 2011, **3**, 1159.
43 F. Dionigi, Z. Zeng, I. Sinev, T. Merzdorf, S. Deshpande, M. B. Lopez, S. Kunze, I. Zegkinoglou, H. Sarodnik, D. Fan, A. Bergmann, J. Drnec, J. F. de Araujo, M. Gliech, D. Teschner, J. Zhu, W.-X. Li, J. Greeley, B. Roldan Cuenya and P. Strasser, *In situ* structure and catalytic mechanism of NiFe and CoFe layered double hydroxides during oxygen evolution, *Nat. Commun.*, 2020, **11**, 2522.
44 P. Zhang, H. Xiang, L. Tao, H. Dong, Y. Zhou, T. S. Hu, X. Chen, S. Liu, S. Wang and S. Garaj, Chemically activated MoS_2 for efficient hydrogen production, *Nano Energy*, 2019, **57**, 535.
45 W. Zhang, X. Zhang, L. Chen, J. Dai, Y. Ding, L. Ji, J. Zhao, M. Yan, F. Yang, C.-R. Chang and S. Guo, Single-Walled Carbon Nanotube Induced Optimized Electron Polarization of Rhodium Nanocrystals To Develop an Interface Catalyst for Highly Efficient Electrocatalysis, *ACS Catal.*, 2018, **8**, 8092.
46 B. Lu, L. Guo, F. Wu, Y. Peng, J. E. Lu, T. J. Smart, N. Wang, Y. Z. Finfrock, D. Morris, P. Zhang, N. Li, P. Gao, Y. Ping and S. Chen, Ruthenium atomically dispersed in carbon outperforms platinum toward hydrogen evolution in alkaline media, *Nat. Commun.*, 2019, **10**, 631.
47 Y. Xu, Y. Fo, H. Lv, X. Cui, G. Liu, X. Zhou and L. Jiang, Anderson-Type Polyoxometalate-Assisted Synthesis of Defect-Rich Doped 1T/2H-MoSe2 Nanosheets for Efficient Seawater Splitting and Mg/Seawater Batteries, *ACS Appl. Mater. Interfaces*, 2022, **14**, 10246.
48 J. Yu, G. Li, H. Liu, L. Zhao, A. Wang, Z. Liu, H. Li, H. Liu, Y. Hu and W. Zhou, Ru-Ru_2P Phi NPC and NPC@RuO_2 Synthesized via Environment-Friendly and Solid-Phase Phosphating Process by Saccharomycetes as N/P Sources and Carbon Template for Overall Water Splitting in Acid Electrolyte, *Adv. Funct. Mater.*, 2019, **29**, 1901154.
49 G. Chen, T. Wang, J. Zhang, P. Liu, H. Sun, X. Zhuang, M. Chen and X. Feng, Accelerated Hydrogen Evolution Kinetics on NiFe-Layered Double Hydroxide Electrocatalysts by Tailoring Water Dissociation Active Sites, *Adv. Mater.*, 2018, **30**, 1706279.
50 B. Ye, L. Huang, Y. Hou, R. Jiang, L. Sun, Z. Yu, B. Zhang, Y. Huang and Y. Zhang, Pt (111) quantum dot decorated flower-like Fe_2O_3 (104) thin film nanosheets as a highly efficient bifunctional electrocatalyst for overall water splitting, *J. Mater. Chem. A*, 2019, **7**, 11379.
51 K. Zhu, J. Chen, W. Wang, J. Liao, J. Dong, M. O. L. Chee, N. Wang, P. Dong, P. M. Ajayan, S. Gao, J. Shen and M. Ye, Etching-Doping Sedimentation Equilibrium Strategy: Accelerating Kinetics on Hollow Rh-Doped CoFe-Layered Double Hydroxides for Water Splitting, *Adv. Funct. Mater.*, 2020, **30**, 2003556.
52 B. H. R. Suryanto, Y. Wang, R. K. Hocking, W. Adamson and C. Zhao, Overall electrochemical splitting of water at the heterogeneous interface of nickel and iron oxide, *Nat. Commun.*, 2019, **10**, 5599.
53 X. Zhong, J. Tang, J. Wang, M. Shao, J. Chai, S. Wang, M. Yang, Y. Yang, N. Wang, S. Wang, B. Xu and H. Pan, 3D heterostructured pure and N-Doped Ni_3S_2/VS_2 nanosheets for high efficient overall water splitting, *Electrochim. Acta*, 2018, **269**, 55.
54 M. Zhao, W. Li, J. Li, W. Hu and C. M. Li, Strong Electronic Interaction Enhanced Electrocatalysis of Metal Sulfide Clusters Embedded Metal-Organic Framework Ultrathin Nanosheets toward Highly Efficient Overall Water Splitting, *Adv. Sci.*, 2020, **7**, 2001965.
55 M. Zhao, H. Li, W. Li, J. Li, L. Yi, W. Hu and C. M. Li, Ru-Doping Enhanced Electrocatalysis of Metal-Organic Framework Nanosheets toward Overall Water Splitting, *Chem. – Eur. J.*, 2020, **26**, 17091.

56 P. Chen, T. Zhou, M. Zhang, Y. Tong, C. Zhong, N. Zhang, L. Zhang, C. Wu and Y. Xie, 3D Nitrogen-Anion-Decorated Nickel Sulfides for Highly Efficient Overall Water Splitting, *Adv. Mater.*, 2017, **29**, 1701584.

57 L. Yu, H. Zhou, J. Sun, F. Qin, F. Yu, J. Bao, Y. Yu, S. Chen and Z. Ren, Cu nanowires shelled with NiFe layered double hydroxide nanosheets as bifunctional electrocatalysts for overall water splitting, *Energy Environ. Sci.*, 2017, **10**, 1820.

58 J. Luo, J.-H. Im, M. T. Mayer, M. Schreier, M. K. Nazeeruddin, N.-G. Park, S. D. Tilley, H. J. Fan and M. Graetzel, Water photolysis at 12.3% efficiency via perovskite photovoltaics and Earth-abundant catalysts, *Science*, 2014, **345**, 1593.

59 G. Zhang, Y.-S. Feng, W.-T. Lu, D. He, C.-Y. Wang, Y.-K. Li, X.-Y. Wang and F.-F. Cao, Enhanced Catalysis of Electrochemical Overall Water Splitting in Alkaline Media by Fe Doping in Ni_3S_2 Nanosheet Arrays, *ACS Catal.*, 2018, **8**, 5431.

60 Q. Wang, M. Ming, S. Niu, Y. Zhang, G. Fan and J.-S. Hu, Scalable Solid-State Synthesis of Highly Dispersed Uncapped Metal (Rh, Ru, Ir) Nanoparticles for Efficient Hydrogen Evolution, *Adv. Energy Mater.*, 2018, **8**, 1801698.

61 Y. Song, J. Cheng, J. Liu, Q. Ye, X. Gao, J. Lu and Y. Cheng, Modulating electronic structure of cobalt phosphide porous nanofiber by ruthenium and nickel dual doping for highly-efficiency overall water splitting at high current density, *Appl. Catal., B*, 2021, **298**, 120488.

62 D. Chen, Z. Pu, R. Lu, P. Ji, P. Wang, J. Zhu, C. Lin, H.-W. Li, X. Zhou, Z. Hu, F. Xia, J. Wu and S. Mu, Ultralow Ru Loading Transition Metal Phosphides as High-Efficient Bifunctional Electrocatalyst for a Solar-to-Hydrogen Generation System, *Adv. Energy Mater.*, 2020, **10**, 2000814.

63 J. Wang, F. Xu, H. Jin, Y. Chen and Y. Wang, Non-Noble Metal-based Carbon Composites in Hydrogen Evolution Reaction: Fundamentals to Applications, *Adv. Mater.*, 2017, **29**, 1605838.